CHEMISTRY OF MATERIALS

Article

pubs.acs.org/cm

Elastic Properties of the Solid Electrolyte $Li_7La_3Zr_2O_{12}$ (LLZO)

Seungho Yu,[†] Robert D. Schmidt,[†] Regina Garcia-Mendez,[‡] Erik Herbert,[∥] Nancy J. Dudney,[⊥] Jeffrey B. Wolfenstine,[#] Jeff Sakamoto,[†,‡] and Donald J. Siegel*[,†,‡,§,○]

[†]Mechanical Engineering Department, [‡]Materials Science & Engineering, and [§]Applied Physics Program, University of Michigan, Ann Arbor, Michigan 48109, United States

[∥]Department of Materials Science and Engineering, Michigan Technological University, Houghton, Michigan 49931, United States

[⊥]Materials Science and Technology Division, Oak Ridge National Laboratory, Oak Ridge, Tennessee 37830, United States

[#]RDRL-SED-C Army Research Laboratory, Adelphi, Maryland 20783, United States

[○]Department of Energy Conversion and Storage, Technical University of Denmark, Fysikvej, Building 309, 2800 Kongens Lyngby, Denmark

Supporting Information

ABSTRACT: The oxide known as LLZO, with nominal composition $Li_7La_3Zr_2O_{12}$, is a promising solid electrolyte for Li-based batteries due to its high Li-ion conductivity and chemical stability with respect to lithium. Solid electrolytes may also enable the use of metallic Li anodes by serving as a physical barrier that suppresses dendrite initiation and propagation during cycling. Prior linear elasticity models of the Li electrode/solid electrolyte interface suggest that the stability of this interface is highly dependent on the elastic properties of the solid separator. For example, dendritic suppression is predicted to be enhanced as the electrolyte's shear modulus increases. In the present study a combination of first-principles calculations, acoustic impulse excitation measurements, and nanoindentation experiments are used to determine the elastic constants and moduli for high-conductivity LLZO compositions based on Al and Ta doping. The calculated and measured isotropic shear moduli are in good agreement and fall within the range of 56−61 GPa. These values are an order of magnitude larger than that for Li metal and far exceed the minimum value (~8.5 GPa) believed to be necessary to suppress dendrite initiation. These data suggest that LLZO exhibits sufficient stiffness to warrant additional development as a solid electrolyte for Li batteries.

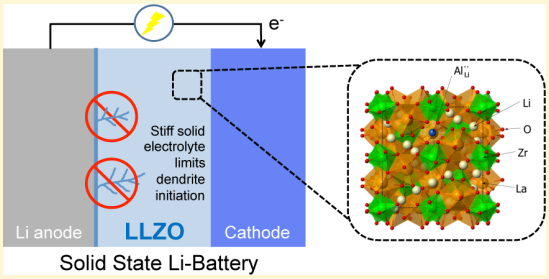

I. INTRODUCTION

Lithium-ion batteries are now widely used in portable electronics and are transitioning to new applications in electric vehicles (EV) and stationary energy storage systems.[1] To accelerate this transition, it is desirable to minimize safety issues associated with conventional organic liquid electrolytes, which are flammable and volatile.[2] For this reason, the development of solid-state electrolytes (SE) is attracting increasing attention, as these compounds have the potential to be nonflammable and stable in contact with the Li metal anode.[3,4] As an additional benefit, solid electrolytes would facilitate increases in energy density by enabling the use of metallic Li anodes. Metallic anodes are envisioned for use in emerging cell chemistries such as Li−air[5] and Li−S, but they could also yield benefits when paired with existing intercalation cathodes.[6]

To be viable, a solid electrolyte should satisfy several performance requirements simultaneously: it should possess high Li-ion conductivity, ~1 mS cm^{-1} or higher, with low electronic conductivity; electrochemical stability against the Li metal anode and state-of-the-art cathodes (5 V or higher vs Li/Li^+) is also essential;[3,7] finally, it should be manufacturable into thin, robust membranes.

Sulfides and oxides are both under consideration as solid electrolytes.[4] Sulfide materials presently exhibit higher ionic conductivities, which has been suggested to arise from the higher polarizability of the sulfide ion.[8] For example, $Li_{10}GeP_2S_{12}$ (LGPS) exhibits a high ionic conductivity of 12 mS cm^{-1} at room temperature.[4] However, sulfides are hygroscopic and form toxic H_2S when exposed to moisture.[9] On the other hand, oxides generally exhibit high chemical stability and ease of handling. At present, the most promising Li-ion conducting oxides are garnets with nominal composition $Li_7La_3Zr_2O_{12}$. Commonly referred to as LLZO, this oxide exhibits a favorable combination of high conductivity (~1 mS cm^{-1}), chemical stability against Li metal, and electrochemical stability (0−6 V vs Li/Li^+).[10−14]

Stoichiometric LLZO adopts a tetragonal crystal structure (space group $Ia\bar{4}d$) at room temperature.[15,16] This polymorph is of less interest for solid electrolyte applications than the cubic polymorph, as the former is limited by low ionic conductivity

Received: September 30, 2015
Revised: December 9, 2015
Published: December 16, 2015

DOI: 10.1021/acs.chemmater.5b03854
Chem. Mater. 2016, 28, 197−206

($\sim 10^{-6}$ S cm^{-1}).[15] However, supervalent doping stabilizes the cubic crystal structure (space group $Ia\bar{3}d$), which has a much higher conductivity, $\sim 10^{-4}$ to 10^{-3} S cm^{-1}.[17] Dopants are expected to increase the degree of vacancy disorder within the Li sublattice, leading to enhanced hopping paths for Li^+ and an increase in conductivity.[18,19] For example, substitution of 0.2−0.24 mol of aluminum (nominal oxidation state of 3+) for lithium creates 0.4−0.48 mol of lithium vacancies per LLZO formula unit, respectively, and stabilizes the cubic phase.[20] In this phase, the ionic conductivity is increased to 0.4 mS cm^{-1} at 298 K. Density functional and molecular dynamics calculations demonstrated that the transition from the tetragonal to cubic phase occurs for Li vacancy concentrations greater than 0.4−0.5 per LLZO formula unit.[16] An alternative to Al doping is substitution of Ta^{5+} on Zr^{4+} sites. Substitution of Ta^{5+} is preferred to Al doping, since Ta, unlike Al, does not reside on the Li sublattice and thus yields higher conductivity.[17] In fact, $Li_{6.5}La_3Zr_{1.5}Ta_{0.5}O_{12}$ (0.5 Li vacancy per formula unit) has achieved a conductivity close to 1 mS cm^{-1} at 298 K.[21]

In addition to possessing high Li-ion conductivity, a viable solid electrolyte should also exhibit appropriate mechanical properties.[22,23] In particular, the elastic moduli of a SE are of key importance. First, it is believed that a SE's shear modulus impacts the tendency for dendrites to form on the anode surface during cycling.[24] Linear elasticity analyses performed by Monroe and Newman suggest that the shear modulus should be at least twice that of Li metal in order to prevent dendrite nucleation.[24] Second, the Young's modulus impacts the fracture strength of a SE. On the basis of Griffith theory, the fracture strength can be estimated using the Young's modulus and the surface energy.[25,26]

Unfortunately, very few investigations of the mechanical properties of LLZO have been reported.[22] Ni et al. measured the room-temperature elastic moduli (Young's modulus, E, shear modulus, G, bulk modulus, B, and Poisson's ratio, ν) of Al-doped cubic LLZO ($Li_{6.24}Al_{0.24}La_3Zr_2O_{11.98}$; volume fraction porosity, P = 0.03) using resonant ultrasound spectroscopy (RUS).[22] The values reported were E = 149.8 GPa, G = 59.6 GPa, and B = 102.8 GPa. On the other hand, the elastic properties of Ta-doped LLZO are not available in the literature. Similarly, an evaluation of the elastic constants of LLZO also appears to be absent.

The present study aims to close these knowledge gaps by determining the elastic constants and moduli for Al- and Ta-doped LLZO (Figure 1) using a combination of first-principles computation and multiple experimental techniques. Nano-indentation experiments were conducted to obtain quasi-single-crystal elastic properties of LLZO; these measurements can be directly compared to values predicted by density functional theory (DFT) calculations. In addition, impulse excitation measurements were used to measure the bulk-scale elastic properties of polycrystalline LLZO. An advantage of impulse excitation is that it directly measures the longitudinal and shear wave speeds by determining the time-of-flight for a single longitudinal or shear pulse. It is, therefore, a simpler alternative to RUS, where wavespeeds are determined by fitting a set of mechanical resonance frequencies to a model. Finally, the elastic properties of metallic Li were revisited computationally. This data was used with the elasticity analyses of Monroe and Newman,[24] and in combination with the measured LLZO elastic properties, to assess the effectiveness of LLZO in suppressing dendrite formation at the Li−LLZO interface.

We find that the predicted and measured elastic properties for LLZO are in excellent agreement. For example, the calculated elastic constants are within 5% of the nano-indentation measurements, with Young's modulus values (E) ranging from 147 to 154 GPa across the Al- and Ta-doped LLZO compositions. Furthermore, the predicted data are consistent with impulse excitation measurements, which capture the polycrystalline microstructure of LLZO specimens; in this case, E values between 140 and 146 GPa were obtained for specimens of relative density greater than 98%. Finally, the measured and calculated shear moduli (G) for Al/Ta-doped LLZO are approximately 60 GPa. This value is more than an order of magnitude larger than that of BCC Li. Hence, on the basis of the model of Monroe,[24] both LLZO compositions may be stiff enough to suppress lithium dendrite formation. These data provide important insights into the mechanical properties of the Li−LLZO interface. Understanding the stability of this interface is a prerequisite for the development of long-lived, all-solid-state batteries.

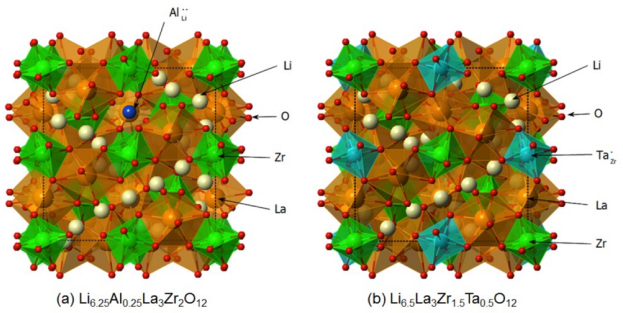

Figure 1. Atomic structure of the computational cells for (a) $Li_{6.25}Al_{0.25}La_3Zr_2O_{12}$ and (b) $Li_{6.5}La_3Zr_{1.5}Ta_{0.5}O_{12}$. Al''_{Li} and $Ta^{\bullet}_{Zr}$ denote, respectively, Al substitution on Li sites and Ta substitution on Zr sites, using Kröger−Vink notation.

II. METHODS

II.A. Computational. All calculations were performed using DFT with a plane wave basis set and the projector augmented wave (PAW)[27,28] method, as implemented in the Vienna *Ab initio* Simulation Package (VASP).[29] The Perdew−Burke−Ernzerhof (PBE)[30] generalized gradient approximation (GGA) was used for the exchange-correlation energy. An energy cutoff of 600 eV was used for the plane wave basis, and the Brillouin zone was sampled using the Monkhorst−Pack scheme.[31] Extensive K-point convergence testing was performed so as to obtain accurate elastic properties. Calculations employing up to a 46 × 46 × 46 k-point mesh (2300 irreducible k-points) were used for metallic Li, and a 4 × 4 × 4 mesh (32 irreducible k-points) was used for LLZO. The convergence criterion for the electronic self-consistency loop was set to 10^{-5} eV (5.32×10^{-5} meV/atom for LLZO), and atomic positions were relaxed (for a specified cell shape and volume) until the forces were less than 0.01 eV Å^{-1}.

Simulation cells were based on the experimental Al-doped[32] and Ta-doped LLZO[18] cubic crystal structures, as shown in Figure 1. These cells contained a total of 188 atoms, corresponding to eight formula units. Li was distributed on the partially occupied 24d and 96h sites using a procedure that excluded occupation of electrostatically unfavorable first nearest-neighbor sites.[12] Before calculating the properties of doped LLZO, we compared the total energies of several pristine LLZO cells containing different distributions of Li ions across the available Li sites. The calculated energy differences among these candidate structures were small (<1.5 meV/atom). The structure having the lowest total energy from this set of candidates was adopted for subsequent calculations. This structure had partial occupancies of 0.542 and 0.448 (equivalent to 13 and 43 atoms in unit cell) for the

DOI: 10.1021/acs.chemmater.5b03854
Chem. Mater. 2016, 28, 197−206

24d and 96h sites, respectively. These occupancies are similar to the experimental values of 0.564 and 0.442 for these sites, respectively.[12]

In the Al-doped structure ($Li_{6.25}Al_{0.25}La_3Zr_2O_{12}$), two randomly selected 24d Li sites were replaced by Al. (Li 24d sites have been previously identified as the most energetically favorable sites for Al doping.[33]) To maintain charge neutrality, a total of four Li atoms located near the Al-sites were also removed from the cell. Likewise, for the Ta-doped structure ($Li_{6.5}La_3Zr_{1.5}Ta_{0.5}O_{12}$), four Zr atoms were replaced by an equivalent number of Ta dopants,[18] and a total of four Li vacancies were created to maintain charge neutrality. The resulting occupancies of the 24d sites are 0.458 (equivalent to 11 Li^+ ions in unit cell) for both the Al- and Ta-doped cells and 0.406 and 0.427 (equivalent to 39 and 41 Li^+ ions in unit cell) for the 96h sites, respectively. To facilitate comparisons with the mechanical properties of a Li anode, the elastic properties of metallic BCC lithium were also investigated.

The elastic properties of a solid phase having a cubic crystal structure can be described using three elastic constants: C_{11}, C_{12}, and C_{44}.[34] The elastic constants were evaluated using Hook's law by calculating the total energy as a function of strain. In addition to being ingredients in the calculation of the elastic and shear moduli (described below), the elastic constants constitute fundamental mechanical properties of a crystalline phase. For example, these data may be useful in follow-on studies involving mesoscale modeling of LLZO-based separators. Three methods were explored for determining the C_{11} and C_{12} elastic constants for LLZO:

Method A: Direct Calculation of C_{11} and the Bulk Modulus, B. In this case, the uniaxial strain, C_{11}, was determined by incrementally expanding or contracting the crystal along a [100] direction (up to ±3% of the minimum-energy lattice constant) and fitting the resulting energy−strain data to a quadratic polynomial. Next, the bulk modulus, B, was obtained by fitting total energy vs volume data to the Murnaghan equation of state.[35] C_{12} was then derived using B and C_{11}, using the relation (1)[34]

$$B = \frac{1}{3}(C_{11} + 2C_{12}) \tag{1}$$

Method B: Direct Calculation of C_{11} and the Difference $C_{11} - C_{12}$. The difference $C_{11} - C_{12}$, defined as Δ_{11-12}, can be independently derived by shearing the crystal with an orthorhombic strain[34]

$$\varepsilon = \begin{bmatrix} \delta & 0 & 0 \\ 0 & -\delta & 0 \\ 0 & 0 & \delta^2/(1-\delta^2) \end{bmatrix} \tag{2}$$

Here, $(\Delta_{11-12})/2$ represents the resistance to a shear stress applied across the (110) plane in the $[1\bar{1}0]$ direction.[36] δ refers to a small strain, which in our calculations is on the order of 0.02. C_{12} can then be obtained using a combination of C_{11} and Δ_{11-12}.

Method C: Direct Calculation of B and Δ_{11-12}. In this case, C_{11} and C_{12} are evaluated using eq 1 and the definition of Δ_{11-12}.

For all methods, C_{44} was obtained by incrementally shearing the crystal with a monoclinic strain[34]

$$\varepsilon = \begin{bmatrix} 0 & \delta/2 & 0 \\ \delta/2 & 0 & 0 \\ 0 & 0 & \delta^2/(4-\delta^2) \end{bmatrix} \tag{3}$$

and fitting to a quadratic polynomial. In this case, δ was varied between −0.03 and +0.03.

Subsequently, the directional properties of the Young's modulus, $E_{[100]}$, $E_{[110]}$, and $E_{[111]}$, and the shear modulus, $G_{[100]}$, $G_{[110]}$, and $G_{[111]}$, were derived from the elastic constants C_{11}, C_{12}, and C_{44} according to[37]

$$E_{[100]} = \frac{(C_{11}-C_{12})(C_{11}+2C_{12})}{(C_{11}+C_{12})},$$
$$E_{[110]} = \frac{4(C_{11}-C_{12})(C_{11}+2C_{12})C_{44}}{2C_{11}C_{44}+(C_{11}-C_{12})(C_{11}+2C_{12})},$$
$$E_{[111]} = \frac{3(C_{11}+2C_{12})C_{44}}{C_{11}+2C_{12}+C_{44}} \tag{4}$$

$$G_{[100]} = C_{44},$$
$$G_{[110]} = \frac{2(C_{11}-C_{12})C_{44}}{C_{11}-C_{12}+2C_{44}},$$
$$G_{[111]} = \frac{3(C_{11}-C_{12})C_{44}}{C_{11}-C_{12}+4C_{44}} \tag{5}$$

These values allow for estimating the anisotropy of the elastic moduli. The polycrystalline isotropic shear modulus, G, was obtained using the calculated elastic constants in combination with the Voigt−Reuss−Hill averaging scheme[37]

$$G = \frac{1}{2}\left[\frac{C_{11}-C_{12}+3C_{44}}{5} + \frac{5C_{44}(C_{11}-C_{12})}{4C_{44}+3(C_{11}-C_{12})}\right] \tag{6}$$

Finally, Young's modulus, E, and Poisson's ratio, ν, assuming an isotropic polycrystalline material, were evaluated using[38]

$$E = \frac{9GB}{3B+G},\quad \nu = \frac{3B-2G}{2(3B+G)} \tag{7}$$

II.B. Experimental. LLZO samples were synthesized from starting powders of Li_2CO_3 (99.0%+, JS-L5940-125, Jade Scientific, Westland, MI), $La(OH)_3$ (99.95%, 43123, Alfa Aesar, Ward Hill, MA), and ZrO_2 nanopowder (99.9%, 40N-0801, Inframet Advanced Materials, Manchester, CT), with doping of either Al_2O_3 (99.9%, AP-212, Mager Scientific, Dexter, MI) or $TaCl_5$ (99.999%, 510688, Aldrich).

Al-doped LLZO with composition $Li_{6.17}Al_{0.28}La_3Zr_2O_3$ was prepared with 7 wt % excess lithium precursor to account for Li loss during calcination. The precursors were mixed in an agate-lined ball mill with 100 g of 10 mm agate media at 350 rpm for 8 h in a planetary ball mill (PM100, Retsch GmbH, Haan, Germany), with 5 min intervals of milling followed by 5 min rest intervals. The mixed powder was cold pressed into 9.40 g pellets of 25.4 mm diameter at 400 kN for 2 min and then calcined on a MgO boat at 1000 °C for 4 h in 0.7 L/min flowing dry air. After calcination, the pellet was manually ground in an agate mortar and pestle and passed through a 75 μm sieve; finally, planetary ball milling was performed for 30 min at 350 rpm.

Ta-doped LLZO of composition $Li_{6.5}La_3Zr_{1.5}Ta_{0.5}O_{12}$ was prepared by adding $TaCl_5$ (previously dissolved in anhydrous ethanol) to the precursors in an agate-milling vial. A 10 wt % excess of lithium precursor was used to compensate for Li loss during synthesis. A planetary ball mill with agate milling media was used to mix the precursors at 350 rpm for 8 h. After milling, the ethanol in the solution was evaporated under an infrared light; the sample was then placed on a MgO boat and heated in air at 150 °C for 2 h. After drying, the powders were collected and cold pressed into a pellet. The pellet was placed in a MgO combustion boat and heated in air at 1000 °C for 4 h. Single phase cubic LLZO was obtained by grinding the pellet into powder and adding 15 wt % of lithium precursor followed by cold pressing and heating a second time at 1000 °C in air for 4 h.

The Al- and Ta-doped bulk specimens of LLZO were hot pressed from 3.5 and 5 g of powder, respectively, in a 12.7 mm diameter graphite die with alumina plungers. Two layers of 0.5 mm graphite foil (99.8%, 42953, Alfa Aesar) were placed between the powder and the plungers to prevent direct contact between the plungers and the powder. The powder was cold pressed at 8 kN for 30 min and then sintered at 1100 °C and 8 kN for 1 h by rapid induction hot pressing (IH15A, Across International, Livingston, NJ). The sintered specimens were each sanded to remove the graphite foil from the surface.

DOI: 10.1021/acs.chemmater.5b03854
Chem. Mater. 2016, 28, 197−206

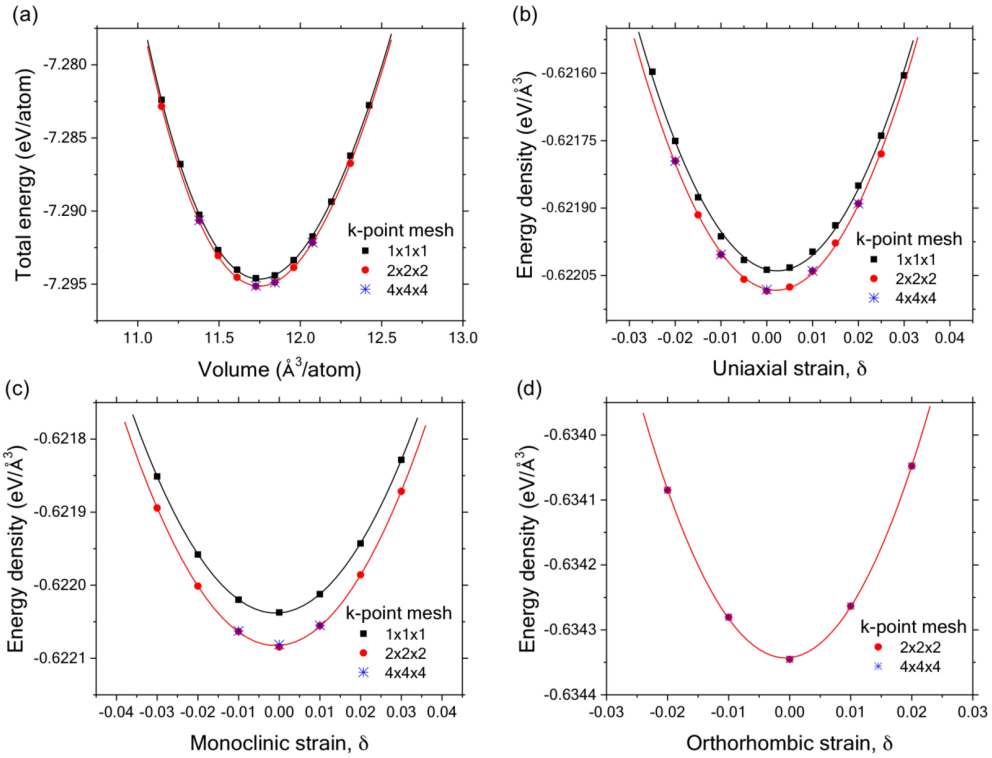

Figure 2. Calculated total energy (or energy density) of Al-doped LLZO as a function of the (a) cell volume, (b) uniaxial strain, (c) monoclinic strain, and (d) orthorhombic strain.

Fractured surfaces of the Al-doped LLZO sintered bulk specimens were mounted on graphite tape and examined by SEM (Nova Nanolab, FEI, Hillsboro, OR) at 15 kV and 0.14 nA using Everhart-Thornley and through-lens secondary electron detectors. Fractured surfaces of the Ta-doped LLZO sintered specimen were mounted on copper tape and examined by SEM (Quanta 200 3D, FEI, Hillsboro, OR) at 15 kV and 0.27 nA.

Lattice parameter and phase purity were determined by Reitveld analysis of X-ray diffraction patterns (Miniflex 600, Rigaku, Tokyo, Japan) with a copper anode and graphite monochromator at 40 kV and 15 mA.

Elastic moduli were measured using two techniques: acoustic impulse excitation and nanoindentation. Acoustic impulse excitation is a nondestructive and rapid technique for measuring bulk, polycrystalline elastic properties. In contrast, nanoidentation examines single grains within the specimen, with results analogous to single-crystal values. Moduli determined by acoustic impulse excitation were calculated from the measured wavespeed (5073PR with M110 lateral transducer, Olympus NDT, Tokyo, Japan) with shear wave couplant (SWC, Olympus NDT). The pulse timing, t, was measured by oscilloscope (PicoScope 2207a, Pico Technologies, Cambridgeshire, UK). The specimen length, l, was measured by micrometer (293-832-30, Mitutoyo, Japan) in five places across each specimen and averaged. Polycrystalline bulk specimens were assumed to be isotropic for calculation of elastic moduli. Longitudinal velocity, V_l, was measured as

$$V_l = \frac{2l}{t_l} \tag{8}$$

Young's modulus, E, and shear modulus, G, were calculated by eqs 9 and 10, using Poisson's ratio, ν = 0.257, from published values[22]

$$E = V_l^2 \rho \frac{(1+\nu)(1-2\nu)}{(1-\nu)} \tag{9}$$

$$G = \frac{E}{2(1+\nu)} \tag{10}$$

Polished Al- and Ta-doped bulk specimens of LLZO were used for nanoindentation measurements. The specimens were polished with a series of diamond compounds to a final grit of 0.5 μm (diamond compound 81-868, extender 811-004, Leco Corp, St. Joseph, MI) on an automatic polishing machine (LP900A, South Bay Technologies, San Clemente, CA). To remove any surface contamination prior to nanoindentation, the specimens were briefly hand polished for 2 min each with the same 0.5 μm diamond compound and thoroughly rinsed with cyclohexane immediately before moving into the nanoindenter.

Nanoindentation experiments were performed using an iNano (Nanomechanics, Inc.) and a diamond Berkovich indenter. The elastic modulus was measured continuously as a function of depth under standard atmospheric conditions by superimposing a small harmonic oscillation in conjunction with the normal load applied to the surface of the test specimen. The harmonic component was driven at 100 Hz with a target oscillation amplitude of 2 nm RMS. The normal loading was controlled such that the loading rate divided by the magnitude of the applied load was held constant at 0.1 s^{-1}, which closely approximates a constant strain rate for a homogeneous test specimen. The Berkovich indenter tip's area function and the measurement system's load frame stiffness, K_{lf}, were experimentally determined using the same load-time history and a fused silica reference. (A fused silica reference is the most commonly used material for determining both the area function and K_{lf}.) E was directly calculated using the Oliver–Pharr method[39] based on these calibrations and the load–displacement stiffness data for LLZO. Additional details regarding the dynamic indentation technique are reported elsewhere.[40,41]

For LLZO, the most accurate estimate of E is obtained from an indentation depth range of approximately 140–230 nm. Data from depths shallower than ~140 nm are more susceptible to errors from thermal drift, contaminants on the surface of the specimen and/or the indenter tip, and potential errors in the area function. Unique to LLZO by virtue of its high E, the data beyond 230 nm are more susceptible to an error in K_{lf}, as the elastic contact stiffness, S, in LLZO at depths beyond 230 nm requires extrapolation of K_{lf}. The extrapolation is potentially problematic because $S \geq K_{lf}$ and under

DOI: 10.1021/acs.chemmater.5b03854
Chem. Mater. 2016, 28, 197–206

Table 1. Elastic Properties of Al- and Ta-Doped LLZO[a]

	C_{11}	C_{12}	C_{44}	B	E	G	ν
				Al-Doped LLZO			
DFT (0 K)	187.0	75.1	71.0	112.4	162.6	64.6	0.26
DFT extrapolated (298 K)					154.5	61.4	
impulse excitation (298 K)				100.2 ± 0.6	146.1 ± 0.8	58.1 ± 0.3	
dynamic nanoindentation (298 K)					150.3 ± 2.2	59.8 ± 0.9	
RUS (298 K) ref 22				102.8 ± 0.3	149.8 ± 0.4	59.6 ± 0.1	0.257 ± 0.002
				Ta-Doped LLZO			
DFT (0 K)	169.8	63.9	69.8	99.2	154.9	62.5	0.24
DFT extrapolated (298 K)					147.2	59.4	
impulse excitation (298 K)				96.0 ± 1.4	139.9 ± 2.1	55.7 ± 0.8	
dynamic nanoindentation (298 K)					153.8 ± 2.7	61.2 ± 1.1	

[a]The elastic constants and moduli are expressed in GPa.

these conditions the calculated E is very sensitive to any potential error in K_{lf}.

III. RESULTS AND DISCUSSION

III.A. Calculated Al-Doped LLZO Elastic Properties. Figure 2a shows the total energy of Al-doped LLZO as a function of cell volume and the associated fit of this data to the Murnaghan equation of state. Similarly, Figure 2b–d shows the total energy as a function of uniaxial, monoclinic, and orthorhombic strains, respectively; solid lines represent fits to a quadratic polynomial. A 2 × 2 × 2 k-point mesh (4 irreducible k-points) was determined to be sufficient to achieve converged values for the bulk modulus and elastic constants; this k-point mesh was also adopted for calculations of the elastic constants, C_{11}, C_{12}, and C_{44}.

As mentioned earlier, three methods were explored for determining the elastic constants. All three approaches employ a direct calculation for C_{44} but then use two different independent quantities to derive the remaining elastic properties (see discussion in Section II). The elastic constants for LLZO derived from these three methods have very similar values, as shown in Table S1. The elastic moduli and Poisson's ratio were derived using eqs 1 and 4–7.

The elastic constants and moduli of Al-doped LLZO are summarized in Table 1. The calculated values were determined using method A (via independent calculations of B, C_{11}, and C_{44}). The calculated B, E, and G at 0 K are 112.4, 162.6, and 64.6 GPa, respectively. The elastic moduli of oxides typically decrease with increasing temperature. Representative decreases for common oxides between 0 and 298 K are ∼4% for MgO,[42] ∼1% for Al_2O_3,[43] and ∼9% for Li_2O.[44] We therefore assume that the calculated moduli of LLZO at 0 K should be reduced by ∼5% to estimate behavior at room temperature. Adopting this scaling factor, we arrive at room-temperature values of 154.5 and 61.4 GPa for E and G, respectively.

III.B. Calculated Ta-Doped LLZO Elastic Properties. Methods A–C were also used to calculate the elastic constants of Ta-doped LLZO. The elastic constants derived from the three methods have very similar values, as shown in Table S2. In Table 1, the calculated B, E, and G evaluated using method A are 99.2, 154.9, and 62.5 GPa, respectively. Assuming a 5% softening of moduli between 0 and 298 K, the predicted values of E and G at room temperature are 147.2 and 59.4 GPa, respectively.

III.C. Measured Elastic Properties of LLZO. Measuring the elastic properties required phase pure, high relative density samples. Hot pressing was used to achieve >98% relative density, and X-ray diffraction was used to characterize the crystal structure. Geometric measurements were used to measure density, whereas SEM fractography was used to evaluate the magnitude and distribution of porosity. Confirming the phase purity and high relative density enabled the elastic property measurement using nanoindentation and impulse excitation to obtain quasi-single-crystal and polycrystalline elastic properties, respectively.

Figure 3 shows X-ray diffraction patterns for the polycrystalline hot pressed samples of Al- and Ta-doped LLZO. The

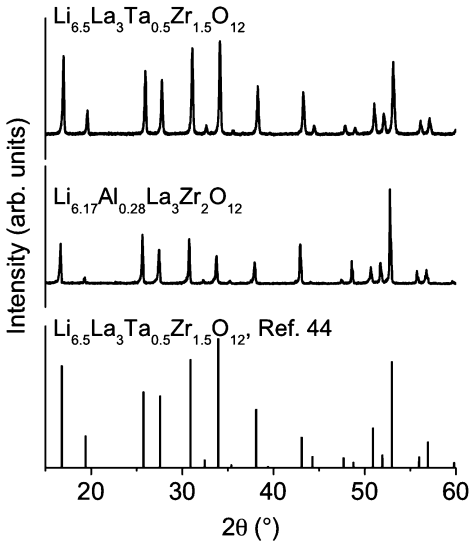

Figure 3. X-ray diffraction patterns of Al- and Ta-doped LLZO.

patterns are consistent with a pure cubic structure with no second phases, as compared to cubic LLZO reported in the literature, $Li_{7-x}La_3Ta_xZr_{2-x}O_{12}$ (ISCD 183686).[45] Lattice constants of 12.957 ± 0.002 and 12.945 ± 0.001 Å for Al- and Ta-doped LLZO, respectively, were determined by Rietveld refinement. (The Bragg-R values obtained from the Reitveld refinement were 29 and 14% for the Al- and Ta-doped LLZO, respectively.) These lattice constant values are in good agreement with the present DFT calculations, which predict lattice constants of 13.023 and 13.013 Å for Al- and Ta-doped LLZO, respectively. Both theory and experiment predict that the Al-doped variant has a slightly larger lattice constant.

The mass density, ρ, of Al- and Ta-doped LLZO hot pressed samples was 5.08 ± 0.09 and 5.34 ± 0.05 g/cm^3, respectively, as

DOI: 10.1021/acs.chemmater.5b03854
Chem. Mater. 2016, 28, 197–206

determined from their mass and physical dimensions. The calculated bulk densities were divided by the theoretical densities (5.139 and 5.396 g/cm^3, respectively), which were determined from the measured lattice parameter. On the basis of these values, the relative density for both compositions is 98.9%. Thus, both materials have near theoretical density. It is well-known that the elastic modulus of a single phase material decreases with increasing porosity.[46] However, given that the density of the LLZO specimens prepared here is near their theoretical densities, the measured E and G of the bulk polycrystalline specimens can be compared directly to the predicted values.

Micrographs of the fractured surfaces of the Al-doped LLZO are shown in Figure 4a. These images further confirm the presence of a dense specimen with nearly zero porosity. Similarly, only limited and isolated porosity was observed in the fractured surfaces of the Ta-doped LLZO specimen, Figure 4b, consistent again with a specimen having near theoretical density.

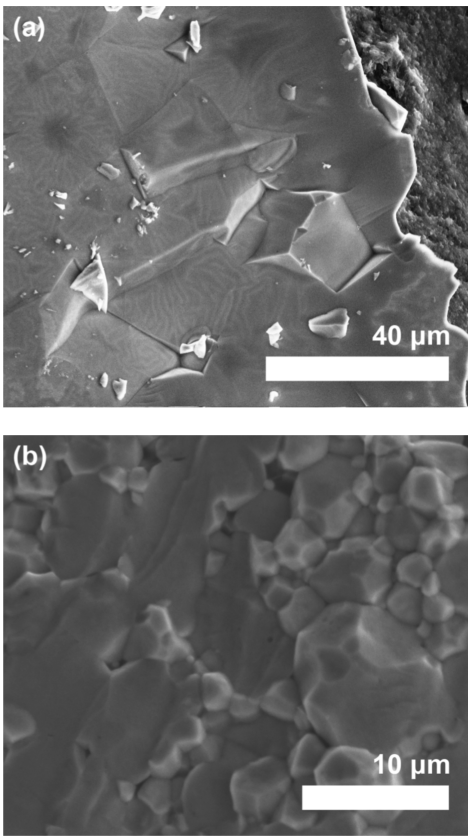

Figure 4. Fracture surfaces of (a) Al-doped and (b) Ta-doped LLZO.

The grain size of the Al-doped LLZO specimen was 5−50 μm, and it was 1−10 μm for the Ta-doped specimen (Figure 4). For each specimen, the grain size is significantly smaller than the specimen length of 2.552 ± 0.007 and 4.135 ± 0.031 mm. Thus, the elastic moduli of the bulk polycrystalline specimens may be assumed to be isotropic.

From nanoindentation, the Young's modulus (E) of the Al-doped LLZO is 150.3 ± 2.2 GPa; for Ta-doped LLZO, a value of 153.8 ± 2.7 GPa was measured (Figure 5 and Table 1). Because the size of each nanoindentation is approximately 500 nm, which is 2−100 times smaller than the diameter of each grain, the elastic moduli values are approximately equivalent to an average over several single-grain/quasi-single-crystal measurements performed on random orientations. Thus, when comparing the calculated (154.5 and 147.2 GPa, respectively) and measured average quasi-single-crystal values, excellent agreement is achieved (Table 1). At 298 K, the Al- and Ta-doped calculated and measured quasi-single-crystal elastic moduli are within 3 and 5%, respectively. Indeed, theory predicts that the Ta-doped LLZO should have a lower elastic modulus compared to that of Al-doped LLZO. However, the relatively small difference in values could be due to experimental error.

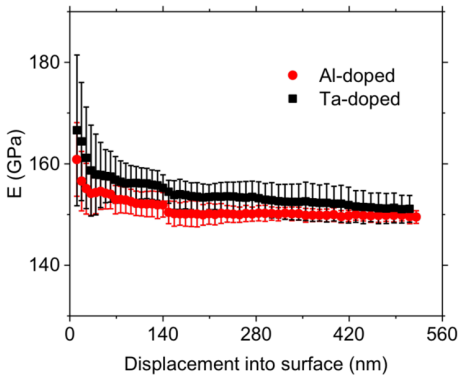

Figure 5. Young's modulus, E, of Al- and Ta-doped LLZO specimens as a function of nanoindentation displacement.

By impulse excitation, the E of the Al-doped LLZO is 146.1 ± 0.8 GPa, and for Ta-doped LLZO, it is 139.9 ± 2.7 GPa (Table 1). Because the impulse excitation technique interrogates the specimen volume beneath the transducer (8 mm diameter) and the grains are <50 μm, the elastic moduli represent isotropic bulk polycrystalline values that include <2% porosity. The error in the elastic moduli is primarily a function of the variation in the specimen thickness.

Experimentally, G measured by nanoindentation is 59.8 ± 0.9 GPa for Al-doped LLZO and 61.2 ± 1.1 GPa for the Ta-doped sample (Table 1). By impulse excitation, G is 58.1 ± 0.3 GPa for Al-doped LLZO and 55.7 ± 0.8 GPa for Ta-doped LLZO (Table 1). Importantly, from Table 1, it can be observed that the calculated and measured (by both impulse excitation and nanoindentation) E and G moduli are within 5%. In addition, from Table 1 it can be observed that experimental and calculated E and G values for Al-doped LLZO are consistent with literature values reported from RUS measurements of similar Al-doped LLZO.[22]

The average of the calculated, nanoindentation, and impulse excitation measurements for E (Table 1 at 298 K) for Al- and Ta-doped LLZO is 150 and 147 GPa, respectively. Using ν = 0.26 (Table 1) and eq 10, these elastic moduli averages give average shear moduli of 60 and 58 GPa for the Al- and Ta-doped LLZO, respectively. The significance of these values will be discussed below after we revisit the shear moduli data for Li.

III.D. Ductility. In addition to being stiff to prevent dendrite penetration, some degree of ductility would also be desirable in a SE so as to maintain good interfacial contact with an electrode during cycling. As a rough estimate of the ductility of LLZO, we have calculated the ratio of the bulk modulus to the shear modulus, B/G, which indicates the ductility/brittleness nature of a solid.[23] According to Pugh's criterion,[47] the critical B/G value for a transition from brittle to ductile behavior is 1.75.

DOI: 10.1021/acs.chemmater.5b03854
Chem. Mater. 2016, 28, 197−206

Table 2. Elastic Properties of BCC Li[a]

	B	C_{11}	C_{12}	C_{44}	E	G	ν
			0 K				
DFT (present study)	13.7	15.3	12.8	11.3	13.0	5.0	0.34
experiment ref 51	13.8	15.4	13.0	11.3	12.9*	4.9*	
experiment ref 52	13.2	14.7	12.5	11.3	12.6*	4.8*	
experiment ref 53	13.1	14.6	12.4	11.4	12.6*	4.8*	
			298 K				
DFT (present study)					11.1	4.25	
experiment ref 52	12.0	13.4	11.3	8.9	10.6*	4.0*	
experiment ref 53	11.9	13.3	11.2	8.8	10.5*	4.0*	
experiment ref 54	12.0	13.4	11.3	8.8	10.5*	4.0*	
experiment ref 55					8.0		
experiment ref 56					4.9		

[a]The elastic constants and moduli are expressed in GPa. Values marked with an asterisk are derived using eqs 6 and 7. DFT values were extrapolated to 298 K by reducing the 0 K values by 15%.

The calculated B/G values for Al- and Ta-doped LLZO are 1.74 and 1.59, respectively. A strict interpretation of Pugh's criterion indicates that both compounds should, therefore, be considered brittle materials. The brittle behavior of both compounds is consistent with the general properties of oxides such as γ-SiO_2, for which B/G = 1.4.[48]

The predicted brittle nature of the two LLZO compositions is in agreement with fracture toughness results of Wolfenstine et al.[49] on Al-doped LLZO ($Li_{6.24}Al_{0.24}La_3Zr_2O_{11.98}$), where a fracture toughness of ~1.25 MPa-$m^{1/2}$ was measured. This value can be compared to fracture toughness values of ~1 MPa-$m^{1/2}$ for an ideal brittle material, such as silicate glass, and 25−35 MPa-$m^{1/2}$ for ductile metals like aluminum.[50]

III.E. BCC Lithium. The calculated elastic constants and moduli for BCC Li are summarized in Tables 2 and S3. Values reported there are for method A. The values for B, C_{11}, and C_{44} at 0 K were obtained using direct DFT calculations, whereas the other elastic properties were derived from those values using eqs 4−7. In Table 2, the calculated values for B, C_{11}, and C_{44} are 13.7, 15.3, and 11.3 GPa, respectively. These values are in very good agreement (differing by only 3%) with the experimental data, which fall within the ranges 13.1−13.8 GPa (B), 14.6−15.4 GPa (C_{11}), and 11.3−11.4 GPa (C_{44}) at 0 K.[51−53] At room temperature, the experimental values are approximately 15% lower.[52−54] Thus, the predicted E and G values are approximately 11.1 and 4.25 GPa, respectively, when extrapolated to room temperature using a similar scaling factor (reduction of 15%).

The predicted value for E of 11.1 GPa at room temperature can be compared to room-temperature experimental values for Li of 8[55] and 4.9 GPa,[56] as determined by resonance spectroscopy and from static bending tests under oil, respectively. The predicted value is reasonable agreement with the resonance value and about twice as high as the static value. It is known that dynamic values are, in general, more accurate than static values as a result of experimental difficulties (e.g., friction at the load points).[57]

III.F. Discussion and Implications. Microstructural features such as (i) porosity, (ii) second phases, (iii) texture, and (iv) grain size can influence the experimental modulus. Although our measured and calculated moduli are in very good agreement, these four features could, in principle, account for differences between theory and experiment. As described above, the LLZO samples examined here are close to theoretical density, contain no second phases (based on X-ray diffraction; Figure 3), and have no texture (based on previous studies of Ni et al.[22] for hot pressed LLZO). This rules out contributions from factors (i)−(iii). Furthermore, it has been previously established that the modulus is independent of grain size and grain boundary characteristics when the grain size is in the micrometer range.[58−61] Since the grain size of both LLZO samples is within this range, 5−50 μm for the Al-doped specimen and 1−10 μm for the Ta-doped specimen, Figure 4, this rules out factor (iv). We therefore conclude that the experimental modulus is not strongly influenced by microstructural features and can be directly compared to the DFT values. Furthermore, our data suggests that variations in the vacancy content of the Li sublattice (brought about by doping with either Al or Ta) do not have a large effect on elastic properties for the doping levels considered here. It appears that contributions from the other sublattices (Zr, O, La) have a larger influence on these properties.

According to the model of Monroe et al., a solid electrolyte having a shear modulus that is a factor of 2 times greater than the shear modulus of metallic Li should suppress dendrite initiation.[24] Given the calculated shear modulus for Li determined in this work (4.25 GPa), a solid electrolyte having a room temperature shear modulus greater than approximately 8.5 GPa is required to suppress dendrite formation. The averaged shear moduli of Al- and Ta-doped LLZO, 58−60 GPa, are more than 10 times greater than the shear modulus of Li and, therefore, could suppress Li dendrite formation. Nevertheless, it is important to recognize that scenarios exist in which dendrites could still form even in the presence of a solid electrolyte that satisfies Monroe's criterion. This could occur, for example, in cases where significant porosity exists at the electrolyte/anode interface. In other words, satisfying Monroe's criterion should be viewed as a necessary, but not sufficient condition for a viable solid electrolyte. As the integrity of the electrode/electrolyte interface is critical, the elastic properties of the electrode materials are also an important factor in the performance of solid-state batteries.

It is instructive to compare the elastic properties of LLZO to those for other solid oxide Li-ion conductors. The Young's modulus for LATP ($Li_{1+x}Al_xTi_{2-x}(PO_4)_3$ with $x \approx 0.3$) determined from stress−strain curves at low strains is approximately 115 GPa.[62] For $Li_{3x}La_{0.67-x}TiO_3$ with $x \approx 0.11$ (LLTO), $E \sim 193$ GPa was determined from nanoindentation and resonant ultrasound spectroscopy.[63] Finally, LiPON thin films have E = 77 GPa, as determined using nanoindentation.[64]

DOI: 10.1021/acs.chemmater.5b03854
Chem. Mater. 2016, 28, 197−206

Thus, the LLZO E value of ~150 GPa reported here is higher than that for LATP and LiPON but smaller than that for LLTO.

LATP and LLTO have both been shown to be unstable in contact with metallic Li because they contain Ti^{4+}, which can be reduced to Ti^{3+}, leading to mixed (both electronic and ionic) conductivity. Unlike LATP and LLTO, LLZO and LiPON are both stable with respect to Li. Moreover, the shear moduli of LLZO (60 GPa) and LiPON (31 GPa) both exceed the critical shear modulus criterion of Monroe and Newman; hence, both of these materials are expected to inhibit Li dendrite initiation. However, since the shear modulus of LLZO is about twice that of LiPON, it is expected that LLZO will have a higher resistance to Li dendrite nucleation during cycling. Furthermore, the Li-ion conductivity of LLZO is about 100−1000 times higher than that of LiPON; hence, LLZO appears to be an optimal choice for a solid Li-ion conducting electrolyte for use with a Li anode.

III.G. Elastic Anisotropy. Both Al- and Ta-doped LLZO exhibit elastic anisotropy: the Young's modulus projected onto the [111] direction is the largest of the three directions, with the [100] projection being the smallest. The $E_{[111]}/E_{[100]}$ ratios are 1.22 and 1.26 for Al- and Ta-doped LLZO, respectively. The Zener anisotropy ratio, A, which is given by $A = 2C_{44}/(C_{11} - C_{12})$, describes the elastic anisotropy of a cubic crystal, with a value of $A = 1$ indicating an isotropic material. For Al- and Ta-doped LLZO, anisotropy ratios of 1.27 and 1.32 were calculated, respectively. To place these values in context, we note that several oxides have high anisotropy ratios: for example, 2.38 for $BaTiO_3$, 2.15 for $MgAl_2O_4$, and 2.14 for UO_2. On the other hand, common isotropic oxides include NiO (1.45), MnO (1.54), and MgO (1.55).[65] Since $A \cong 1$ for Al- and Ta-doped LLZO, we conclude that their elastic properties are relatively isotropic.

IV. CONCLUSIONS

High ionic conductivity is a necessary, but not sufficient, condition for a viable solid electrolyte: to enable use of a metallic lithium anode, such an electrolyte must also be stiff enough to suppress Li dendrite formation during cycling. Consequently, the elastic properties of the solid electrolyte are a highly important—yet occasionally overlooked—feature in the design of all-solid-state batteries. The present study examines the elastic properties of near theoretical density Al- and Ta-doped LLZO using impulse excitation, nanoindentation, and DFT calculations. Due to their high Li-ion conductivities, these compositions are among the most promising solid electrolytes known.

The linear elasticity model of Monroe and Newman suggests that a solid electrolyte having a shear modulus greater than approximately 8.5 GPa can suppress dendrite formation on a Li anode. The present experiments and calculations yield an averaged shear moduli for Al- and Ta-doped LLZO of 58−60 GPa, far exceeding the targeted value.

In addition to characterizing elastic moduli, calculations were also performed to evaluate the brittle/ductile nature of LLZO and its degree of elastic anisotropy. The ratio of the bulk modulus to the shear modulus, B/G, indicates the ductile/brittle nature of a solid. According to Pugh's criterion, the critical B/G value for a transition from brittle to ductile behavior is 1.75. The calculated B/G values for Al- and Ta-doped LLZO are 1.74 and 1.59, respectively, indicating that these compounds are intrinsically brittle, in agreement with fracture toughness data from the literature. Regarding anisotropy, the Zener anisotropy ratio, A, which describes the elastic anisotropy of a cubic crystal, was evaluated for both LLZO variants. In both cases, the elastic properties were found to be relatively isotropic, $A \cong 1$, in agreement with other isotropic oxides such as NiO (1.45) and MgO (1.55).

The high shear moduli reported here suggest that an LLZO-based solid electrolyte could enable long-lived Li-metal batteries. Our analysis sets the stage for further research and development of this promising material.

■ ASSOCIATED CONTENT

Supporting Information

The Supporting Information is available free of charge on the ACS Publications website at DOI: 10.1021/acs.chemmater.5b03854.

Tabulated elastic properties of Al-doped LLZO, Ta-doped LLZO, and BCC Li from DFT calculations (PDF)

■ AUTHOR INFORMATION

Corresponding Author

*E-mail: djsiege@umich.edu. Tel.: 734-764-4808.

Notes

The authors declare no competing financial interest.

■ ACKNOWLEDGMENTS

This work was supported by the U.S. Department of Energy (DOE), Office of Energy Efficiency and Renewable Energy (EERE), Vehicle Technologies Office (VTO) and Advanced Battery Material Research (BMR) programs. Grant no. DE-EE00006821 supported the computational work conducted by S.Y. and D.J.S. as well as the sample preparation and impulse excitation experiments conducted by R.D.S., R.G.-M., J.W., and J.S. Grant no. DE-EE0991-1663 supported the nanoindentation measurements conducted by E.H. and N.J.D. S.Y. acknowledges support from the Kwanjeong Educational Foundation. J.B.W. acknowledges support from the Army Research Laboratory. D.J.S. acknowledges DTU Energy, the Villum Foundation's Visiting Professor Program, and the Nordea Foundation's Residence Program for support during his stay at DTU. The SEM used in this study was obtained with the support of NSF grant no. DMR-0320740.

■ REFERENCES

(1) Bruce, P. G.; Freunberger, S. A.; Hardwick, L. J.; Tarascon, J.-M. Li-O_2 and Li-S Batteries with High Energy Storage. *Nat. Mater.* **2011**, *11*, 19−29.

(2) Roth, E. P.; Orendorff, C. J. How Electrolytes Influence Battery Safety. *Electrochem. Soc. Interface* **2012**, *21*, 45−49.

(3) Goodenough, J. B.; Kim, Y. Challenges for Rechargeable Li Batteries. *Chem. Mater.* **2010**, *22*, 587−603.

(4) Kamaya, N.; Homma, K.; Yamakawa, Y.; Hirayama, M.; Kanno, R.; Yonemura, M.; Kamiyama, T.; Kato, Y.; Hama, S.; Kawamoto, K.; Mitsui, A. A Lithium Superionic Conductor. *Nat. Mater.* **2011**, *10*, 682−686.

(5) Radin, M. D.; Siegel, D. J. Non-Aqueous Metal-Air Batteries: Past, Present, and Future, Chapter 18. In Rechargeable Batteries: Materials, Technologies and New Trends. Zhang, Z., Zhang, S. S., Eds. Springer: Switzerland, 2015, 511.

(6) Adams, S.; Rao, R. P. Ion Transport and Phase Transition in $Li_{7-x}La_3(Zr_{2-x}M_x)O_{12}$ (M = Ta^{5+}, Nb^{5+}, x = 0, 0.25). *J. Mater. Chem.* **2012**, *22*, 1426−1434.

DOI: 10.1021/acs.chemmater.5b03854
Chem. Mater. 2016, 28, 197−206

(7) Miara, L. J.; Ong, S. P.; Mo, Y.; Richards, W. D.; Park, Y.; Lee, J.-M.; Lee, H. S.; Ceder, G. Effect of Rb and Ta Doping on the Ionic Conductivity and Stability of the Garnet $Li_{7+2x-y}(La_{3-x}Rb_x)(Zr_{2-y}Ta_y)O_{12}$ ($0 \le x \le 0.375$, $0 \le y \le 1$) Superionic Conductor: A First Principles Investigation. *Chem. Mater.* **2013**, *25*, 3048−3055.
(8) Kanno, R.; Hata, T.; Kawamoto, Y.; Irie, M. Synthesis of a New Lithium Ionic Conductor, Thio-LISICON−Lithium Germanium Sulfide System. *Solid State Ionics* **2000**, *130*, 97−104.
(9) Muramatsu, H.; Hayashi, A.; Ohtomo, T.; Hama, S.; Tatsumisago, M. Structural Change of $Li_2S-P_2S_5$ Sulfide Solid Electrolytes in the Atmosphere. *Solid State Ionics* **2011**, *182*, 116−119.
(10) Murugan, R.; Thangadurai, V.; Weppner, W. Fast Lithium Ion Conduction in Garnet-Type $Li_7La_3Zr_2O_{12}$. *Angew. Chem., Int. Ed.* **2007**, *46*, 7778−7781.
(11) Kotobuki, M.; Munakata, H.; Kanamura, K.; Sato, Y.; Yoshida, T. Compatibility of $Li_7La_3Zr_2O_{12}$ Solid Electrolyte to All-Solid-State Battery Using Li Metal Anode. *J. Electrochem. Soc.* **2010**, *157*, A1076−A1079.
(12) Xie, H.; Alonso, J. A.; Li, Y.; Fernández-Díaz, M. T.; Goodenough, J. B. Lithium Distribution in Aluminum-Free Cubic $Li_7La_3Zr_2O_{12}$. *Chem. Mater.* **2011**, *23*, 3587−3589.
(13) Geiger, C. A.; Alekseev, E.; Lazic, B.; Fisch, M.; Armbruster, T.; Langner, R.; Fechtelkord, M.; Kim, N.; Pettke, T.; Weppner, W. Crystal Chemistry and Stability of "$Li_7La_3Zr_2O_{12}$" Garnet: A Fast Lithium-Ion Conductor. *Inorg. Chem.* **2011**, *50*, 1089−1097.
(14) Kc, S.; Longo, R. C.; Xiong, K.; Cho, K. Point defects in garnet-type solid electrolyte (c-$Li_7La_3Zr_2O_{12}$) for Li-ion batteries. *Solid State Ionics* **2014**, *261*, 100−105.
(15) Awaka, J.; Kijima, N.; Hayakawa, H.; Akimoto, J. Synthesis and Structure Analysis of Tetragonal $Li_7La_3Zr_2O_{12}$ with the Garnet-Related Type Structure. *J. Solid State Chem.* **2009**, *182*, 2046−2052.
(16) Bernstein, N.; Johannes, M. D.; Hoang, K. Origin of the Structural Phase Transition in $Li_7La_3Zr_2O_{12}$. *Phys. Rev. Lett.* **2012**, *109*, 205702.
(17) Allen, J. L.; Wolfenstine, J.; Rangasamy, E.; Sakamoto, J. Effect of Substitution (Ta, Al, Ga) on the Conductivity of $Li_7La_3Zr_2O_{12}$. *J. Power Sources* **2012**, *206*, 315−319.
(18) Thompson, T.; Wolfenstine, J.; Allen, J. L.; Johannes, M.; Huq, A.; David, I. N.; Sakamoto, J. Tetragonal vs. Cubic Phase Stability in Al - free Ta Doped $Li_7La_3Zr_2O_{12}$ (LLZO). *J. Mater. Chem. A* **2014**, *2*, 13431−13436.
(19) Mukhopadhyay, S.; Thompson, T.; Sakamoto, J.; Huq, A.; Wolfenstine, J.; Allen, J. L.; Bernstein, N.; Stewart, D. A.; Johannes, M. D. Structure and Stoichiometry in Supervalent Doped $Li_7La_3Zr_2O_{12}$. *Chem. Mater.* **2015**, *27*, 3658−3665.
(20) Rangasamy, E.; Wolfenstine, J.; Sakamoto, J. The role of Al and Li concentration on the formation of cubic garnet solid electrolyte of nominal composition $Li_7La_3Zr_2O_{12}$. *Solid State Ionics* **2012**, *206*, 28−32.
(21) Thompson, T.; Sharafi, A.; Johannes, M. D.; Huq, A.; Allen, J. L.; Wolfenstine, J.; Sakamoto, J. A Tale of Two Sites: On Defining the Carrier Concentration in Garnet-Based Ionic Conductors for Advanced Li Batteries. *Adv. Energy Mater.* **2015**, *5*, 1500096.
(22) Ni, J.; Case, E.; Sakamoto, J.; Rangasamy, E.; Wolfenstine, J. Room Temperature Elastic Moduli and Vickers Hardness of Hot-Pressed LLZO Cubic Garnet. *J. Mater. Sci.* **2012**, *47*, 7978−7985.
(23) Wang, Z. Q.; W, M. S.; Liu, G.; Lei, X. L.; Xu, B.; Ouyang, C. Y. Elastic Properties of New Solid State Electrolyte Material $Li_{10}GeP_2S_{12}$: A Study from First-Principles Calculations. *Int. J. Electrochem. Sci.* **2014**, *9*, 562−568.
(24) Monroe, C.; Newman, J. The Impact of Elastic Deformation on Deposition Kinetics at Lithium/Polymer Interfaces. *J. Electrochem. Soc.* **2005**, *152*, A396−A404.
(25) Miannay, D. P. *Fracture Mechanics*; Springer: New York, 1998.
(26) Sakanoi, R.; Shimazaki, T.; Xu, J.; Higuchi, Y.; Ozawa, N.; Sato, K.; Hashida, T.; Kubo, M. Communication: Different Behavior of Young's Modulus and Fracture Strength of CeO_2: Density Functional Theory Calculations. *J. Chem. Phys.* **2014**, *140*, 121102.
(27) Blöchl, P. E. Projector Augmented-Wave Method. *Phys. Rev. B: Condens. Matter Mater. Phys.* **1994**, *50*, 17953−17979.
(28) Kresse, G.; Joubert, D. From Ultrasoft Pseudopotentials to the Projector Augmented-Wave Method. *Phys. Rev. B: Condens. Matter Mater. Phys.* **1999**, *59*, 1758−1775.
(29) Kresse, G.; Furthmüller, J. Efficient Iterative Schemes for Ab Initio Total-Energy Calculations Using a Plane-Wave Basis Set. *Phys. Rev. B: Condens. Matter Mater. Phys.* **1996**, *54*, 11169−11186.
(30) Perdew, J. P.; Burke, K.; Ernzerhof, M. Generalized Gradient Approximation Made Simple. *Phys. Rev. Lett.* **1996**, *77*, 3865−3868.
(31) Monkhorst, H. J.; Pack, J. D. Special Points for Brillouin-Zone Integrations. *Phys. Rev. B* **1976**, *13*, 5188−5192.
(32) Li, Y.; Han, J.-T.; Wang, C.-A.; Vogel, S. C.; Xie, H.; Xu, M.; Goodenough, J. B. Ionic Distribution and Conductivity in Lithium Garnet $Li_7La_3Zr_2O_{12}$. *J. Power Sources* **2012**, *209*, 278−281.
(33) Rettenwander, D.; Blaha, P.; Laskowski, R.; Schwarz, K.; Bottke, P.; Wilkening, M.; Geiger, C. A.; Amthauer, G. DFT Study of the Role of Al^{3+} in the Fast Ion-Conductor $Li_{7-3x}Al_{3+x}La_3Zr_2O_{12}$ Garnet. *Chem. Mater.* **2014**, *26*, 2617−2623.
(34) Mehl, M. J.; Osburn, J. E.; Papaconstantopoulos, D. A.; Klein, B. M. Structural Properties of Ordered High-Melting-Temperature Intermetallic Alloys from First-Principles Total-Energy Calculations. *Phys. Rev. B: Condens. Matter Mater. Phys.* **1990**, *41*, 10311−10323.
(35) Murnaghan, F. D. The Compressibility of Media under Extreme Pressures. *Proc. Natl. Acad. Sci. U. S. A.* **1944**, *30*, 244−247.
(36) Ranganathan, S. I.; Ostoja-Starzewski, M. Universal Elastic Anisotropy Index. *Phys. Rev. Lett.* **2008**, *101*, 055504.
(37) Chung, D.-H.; Swica, J. J.; Crandall, W. B. Relation of Single-Crystal Elastic Constants to Polycrystalline Isotropic Elastic Moduli of MgO. *J. Am. Ceram. Soc.* **1963**, *46*, 452−457.
(38) Uesugi, T.; Takigawa, Y.; Higashi, K. Elastic constants of AlLi from first principles. *Mater. Trans.* **2005**, *46*, 1117−1121.
(39) Oliver, W. C.; Pharr, G. M. An Improved Technique for Determining Hardness and Elastic Modulus Using Load and Displacement Sensing Indentation Experiments. *J. Mater. Res.* **1992**, *7*, 1564−1583.
(40) Hay, J.; Agee, P.; Herbert, E. Continuous Stiffness Measurement during Instrumented Indentation Testing. *Exp. Technol.* **2010**, *34*, 86−94.
(41) Herbert, E. G.; Johanns, K. E.; Singleton, R. S.; Pharr, G. M. On the Measurement of Energy Dissipation Using Nanoindentation and the Continuous Stiffness Measurement Technique. *J. Mater. Res.* **2013**, *28*, 3029−3042.
(42) Marklund, K.; Mahmoud, S. A. Elastic Constants of Magnesium Oxide. *Phys. Scr.* **1971**, *3*, 75−76.
(43) Wachtman, J. B.; Tefft, W. E.; Lam, D. G.; Apstein, C. S. Exponential Temperature Dependence of Young's Modulus for Several Oxides. *Phys. Rev.* **1961**, *122*, 1754−1759.
(44) Dovesi, R.; Roetti, C.; Freyria-Fava, C.; Prencipe, M.; Saunders, V. R. On the Elastic Properties of Lithium, Sodium and Potassium Oxide. An Ab Initio Study. *Chem. Phys.* **1991**, *156*, 11−19.
(45) Logéat, A.; Köhler, T.; Eisele, U.; Stiaszny, B.; Harzer, A.; Tovar, M.; Senyshyn, A.; Ehrenberg, H.; Kozinsky, B. From Order to Disorder: The Structure of Lithium-Conducting Garnets $Li_{7-x}La_3Ta_xZr_{2-x}O_{12}$ (x = 0−2). *Solid State Ionics* **2012**, *206*, 33−38.
(46) Rice, R. W. *Porosity of Ceramics*; Marcel Dekker: New York, 1998.
(47) Pugh, S. F. Relations between the Elastic Moduli and the Plastic Properties of Polycrystalline Pure Metals. *London Edinb. Dubl. Philos. Mag.* **1954**, *45*, 823−843.
(48) Niu, H.; Chen, X.-Q.; Liu, P.; Xing, W.; Cheng, X.; Li, D.; Li, Y. Extra-Electron Induced Covalent Strengthening and Generalization of Intrinsic Ductile-to-Brittle Criterion. *Sci. Rep.* **2012**, *2*, 718.
(49) Wolfenstine, J.; Jo, H.; Cho, Y.-H.; David, I. N.; Askeland, P.; Case, E. D.; Kim, H.; Choe, H.; Sakamoto, J. A Preliminary Investigation of Fracture Toughness of $Li_7La_3Zr_2O_{12}$ and its Comparison to Other Solid Li-Ion Conductors. *Mater. Lett.* **2013**, *96*, 117−120.

DOI: 10.1021/acs.chemmater.5b03854
Chem. Mater. 2016, 28, 197−206

(50) Chiang, Y.-M.; Birnie, D.; Kingery, W. D. *Physical Ceramics*; John Wiley & Sons: New York, 1997.
(51) Nash, H. C.; Smith, C. S. Single-Crystal Elastic Constants of Lithium. *J. Phys. Chem. Solids* **1959**, *9*, 113−118.
(52) Slotwinski, T.; Trivisonno, J. Temperature Dependence of the Elastic Constants of Single Crystal Lithium. *J. Phys. Chem. Solids* **1969**, *30*, 1276−1278.
(53) Day, J. P.; Ruoff, A. L. The Variation of the Elastic Constants of Lithium with Temperature and Pressure. *Phys. Status Solidi A* **1974**, *25*, 205−213.
(54) Felice, R. A.; Trivisonno, J.; Schuele, D. E. Temperature and Pressure Dependence of the Single-Crystal Elastic Constants of ^{6}Li and Natural Lithium. *Phys. Rev. B* **1977**, *16*, 5173−5184.
(55) Robertson, W. M.; Montgomery, D. J. Elastic Modulus of Isotopically-Concentrated Lithium. *Phys. Rev.* **1960**, *117*, 440−442.
(56) Bridgman, P. W. The Effect of Tension on the Electrical Resistance of Certain Abnormal Metals. *Proc. Am. Acad. Arts Sci.* **1922**, *57*, 41−66.
(57) Huntington, H. B.; Seitz, F.; Turnbull, D. *Solid State Physics: Advances in Research and Applications*; Academic Press: New York, 1958.
(58) Chaim, R.; Hefetz, M. Effect of Grain Size on Elastic Modulus and Hardness of Nanocrystalline ZrO_2-3 wt% Y_2O_3 Ceramic. *J. Mater. Sci.* **2004**, *39*, 3057−3061.
(59) Fryxell, R. E.; Chandler, B. A. Creep, Strength, Expansion, and Elastic Moduli of Sintered BeO as a Function of Grain Size, Porosity, and Grain Prientation. *J. Am. Ceram. Soc.* **1964**, *47*, 283−291.
(60) Vasilos, T.; Mitchell, J. B.; Spriggs, R. M. Mechanical Properties of Pure, Dense Magnesium Oxide as a Function of Temperature and Grain Size. *J. Am. Ceram. Soc.* **1964**, *47*, 606−610.
(61) Davidge, R. W.; Evans, A. G. The Strength of Ceramics. *Mater. Sci. Eng.* **1970**, *6*, 281−298.
(62) Jackman, S. D.; Cutler, R. A. Effect of Microcracking on Ionic Conductivity in LATP. *J. Power Sources* **2012**, *218*, 65−72.
(63) Cho, Y.-H.; Wolfenstine, J.; Rangasamy, E.; Kim, H.; Choe, H.; Sakamoto, J. Mechanical Properties of the Solid Li-Ion Conducting Electrolyte: $Li_{0.33}La_{0.57}TiO_3$. *J. Mater. Sci.* **2012**, *47*, 5970−5977.
(64) Herbert, E. G.; Tenhaeff, W. E.; Dudney, N. J.; Pharr, G. M. Mechanical Characterization of LiPON Films Using Nanoindentation. *Thin Solid Films* **2011**, *520*, 413−418.
(65) Rice, R. W. Possible Effects of Elastic Anisotropy on Mechanical Properties of Ceramics. *J. Mater. Sci. Lett.* **1994**, *13*, 1261−1266.

DOI: 10.1021/acs.chemmater.5b03854
Chem. Mater. 2016, 28, 197−206